



Fabrication of core–shell structured $\text{TiO}_2@\text{Sb-SnO}_2$ with improved electroconductivity

Yanan Wang¹ , Jianhua Qian^{2,*} , Jinjuan Xing¹ , Jiasheng Xu¹ , Lin Liu¹ , and Kunyi Ma¹

¹Liaoning Province Key Laboratory for Functional Compounds Synthesis and Application, College of Chemistry and Chemical Engineering, Bohai University, Jinzhou 121013, China

²School of Petrochemical Engineering, College of Chemistry, Chemical Engineering and Environmental Engineering, Liaoning Shihua University, Fushun 113001, China

Received: 9 July 2019

Accepted: 13 November 2019

Published online:
19 November 2019

© Springer Science+Business Media, LLC, part of Springer Nature 2019

ABSTRACT

TiO_2 can be integrated with antimony-doped tin oxide to obtain composite materials with high electroconductivity. Based on this, spherical $\text{TiO}_2@\text{Sb-SnO}_2$ (TSS) has been prepared by homogeneous precipitation combined with a high-temperature calcination process. The morphology, structure and composition of TSS were characterized by scanning electron microscope, Brunauer–Emmet–Teller surface area analyzer, X-ray diffractometer and transmission electron microscope with energy-dispersive X-ray spectrometer, respectively. Effects of dropping conditions, introducing sulfate, pH value, calcination temperature and holding time on the conductivity of TSS were investigated by measuring resistivity, Zeta potential and particle size, meanwhile the calcination action and conductive mechanism by thermogravimetric analysis, X-ray photoelectron spectroscopy and electron spin resonance. The results revealed that the core–shell structured TSS was formed, and the resistivity of composite powder was below $4.0 \Omega \text{ cm}$ under the optimum conditions. Our analysis indicates that the conductive channel mechanism is the main conductive mechanism of the as-prepared composite.

Introduction

Core–shell (CS) nanoparticles (NPs) were first reported in early 1990's [1], which have improved optical, catalytic, electronic, magnetic properties and other physicochemical properties in various applications, for example, catalysis [2–4], lithium ion battery

[5], soft magnetic composites [6] and targeted drug delivery [7]. In order to exhibit extraordinary or new properties, the research directions have been diversifying in different shapes [8–10], multi shells [5] and so on, ascribing to the synergism between core and shell materials. Therefore, the appropriate design of CS-structured materials with different properties is the primary objective of material investigators.

Address correspondence to E-mail: qianjianhua@bhu.edu.cn

The reported preparation methods of CS composite powder mainly conclude mechanical aggregation method (ball-milling dispersion [11] and ultrasonic dispersion [12]) one-step hydrothermal synthesis [9], polymer-pyrolysis method [13] and matrix coating methods including co-precipitation [14–16], polymeric precursor method [17, 18] (Pechini route [19]), homogeneous precipitation [2, 20, 21], etc. Among these methods, powder coating technology has impacts on a great variety of composite powder [22], in which homogeneous precipitation method has been extensively employed because it can efficiently regulate the size and shape of particles for the synthesis of superfine oxides and other composite materials by slow hydrolysis of the precipitant in the reaction mixture [2].

Inorganic pigment fillers have the broad use in the production of paints, plastics, ceramics and many other applied materials to improve, enhance and endow new functions [23]. However, there are electrostatic hazards due to impact, extrusion and friction with each other of these materials, such as fire, explosion and electromagnetic interference caused by electrostatic discharge [24] as well as adsorption of dust and product bonding resulted from electrostatic attraction. Thus, research and development as well as application of conductive filler are crucial. It has been reported that the inorganic/inorganic particle-coating technology for surface modification was carried out to improve electrical conductivity of the matrix fillers, which was based on cheap mineral fillers, such as kaolinite [14], talc [15], barite [16], clay [19], wollastonite [25] and titanium dioxide (TiO_2) [26]. Among them, pigment-grade TiO_2 with the particle diameter of 200–300 nm, typically of rutile phase, has been widely acted as the matrix of composite powder because of its superior scattering property (compared with all other white pigments) and unique chemical durability as well as innocuity [27, 28]. Meanwhile, antimony-doped tin dioxide (ATO) is well-known transparent conductive oxide because of high conductivity, optical transparency, excellent IR blocking property, chemical and thermal stability [10, 11, 19], while the high cost and the dark gray color of ATO materials result in an undesirable appearance to the final product. Hence, with TiO_2 as the core and ATO as a conductive nanoshell of the coated composite, the advantages of the two materials can be fully utilized to prepare light colored conductive inorganic composite fillers. The composite materials have a

more great application prospect than traditional conductive materials including metal [29], carbon materials [30], metal oxides [31] and so on.

In the present work, we adopted homogeneous precipitation to fabricate the preliminary CS precursor that was subsequently calcined to obtain the CS-structured $\text{TiO}_2@\text{Sb-SnO}_2$ (TSS) composite conductive powder. We also have discussed the influence of main factors on the structure and resistivity of the samples based on the selection of optimal parameters, including the conditions of dropping and calcination, the kinds and amounts of sulfate as well as pH value. And the conductive mechanism of composite powder was finally investigated.

Experimental

Materials

All the chemicals used are of analytical grade without further purification, including tin(IV) chloride pentahydrate ($\text{SnCl}_4 \cdot 5\text{H}_2\text{O}$), antimony trichloride (SbCl_3), sodium sulfate (Na_2SO_4), potassium sulfate (K_2SO_4), ammonium sulfate ($(\text{NH}_4)_2\text{SO}_4$), urea (CON_2H_4), cetyltrimethyl ammonium bromide (CTAB, $\text{C}_{16}\text{H}_{33}(\text{CH}_3)_3\text{NBr}$), hydrochloric acid (HCl) and anhydrous ethanol ($\text{C}_2\text{H}_5\text{OH}$). TiO_2 (Jinzhou titanium industry Co. Ltd., China).

Preparation of $\text{TiO}_2@\text{Sb-SnO}_2$ composite

$\text{TiO}_2@\text{Sb-SnO}_2$ conductive nanocomposite was prepared as follows. In a typical procedure, 0.15 mol of urea and 0.16 mmol (0.075 wt%) CTAB were dissolved in 80 mL deionized water and stirred for 30 min; then 0.025 mol TiO_2 was added under continuously stirred conditions. The suspension containing TiO_2 (Suspension A) was ultrasound dispersed for 1 h, and then transferred to a 250 mL three-necked, round-bottomed flask. Meanwhile, 4.5 mmol $(\text{NH}_4)_2\text{SO}_4$ were taken in the flask. When the temperature rise to 60 °C, 0.20 mol L^{-1} mixed hydrochloric acid solution of $\text{SnCl}_4 \cdot 5\text{H}_2\text{O}$ and SbCl_3 (Solution B, $n(\text{Sn})/n(\text{Sb}) = 12$) were added dropwise slowly to the above mixture by peristaltic pump. After that, the seriflux was refluxed under vigorous stirring for 6–10 h at 95 °C to pH = 5. The resulting pale yellow precipitates were washed two to three times with deionized water and anhydrous ethanol,

respectively, to remove Cl^- (test by AgNO_3). The precursors were subsequently dried at 90°C for 12 h and were finally calcined at 550°C for 2 h in the air at a heating rate of $15^\circ\text{C min}^{-1}$ to obtain TSS composite particles. The fabrication process of conductive composite powder is shown in Fig. 1.

Sample characterization

Surface morphology and microstructure of the samples prepared were observed with a field emission scanning electron microscope (FESEM, S-4800, Hitachi Co., Japan). TEM, HRTEM and TEM elemental mapping images were obtained from a transmission electron microscope (TEM, JEM-2100F, JEOL Co., Japan) equipped with an energy-dispersive X-ray spectrometer (EDS) analyzer. The crystal phases of the synthesized samples were acquired with an X-ray diffractometer (XRD, Ultima IV, Rigaku Co., Japan) with $\text{Cu K}\alpha$ radiation and 2θ ranging from 10° to 80° at a scanning rate of 0.2° s^{-1} . Surface compositions and chemical states analysis of composite powers were examined by X-ray photoelectron spectroscopy (XPS, K-Alpha, Thermo Scientific Co., USA). Electron paramagnetic resonance (ESR) studies of the uncalcined precursors and calcined samples were tested by JEOL JES-FA200 ESR spectrometer. The particle size distribution of powder and Zeta potential of diluted samples was measured on the Nano-ZS90 particle size analyzer. Thermogravimetric analysis (TGA) measurements (Pyris Diamond, Perkin-Elmer Co., USA) were carried out on the uncalcined precursors from 30°C to 900°C in the air atmosphere at a heating rate of $10^\circ\text{C min}^{-1}$. The Brunauer–Emmet–Teller (BET) specific surface area of samples was measured at 77 K using a surface area analyzer (Autosorb-iQ-MP/RX, Quantachrome, USA). The

brightness of different samples was measured by CM-3600d whiteness instrument (Minolta Co., Japan).

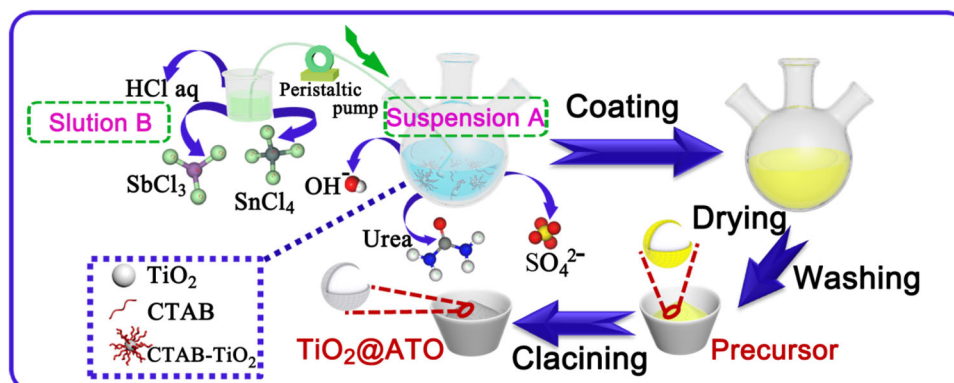
The resistivity of the coated TiO_2 powder was measured on the RTS-8 four-point probe resistivity measurement system (Guangzhou, China). Because of the powdery samples, powder density and contacts among granules have influence on the measured resistivity of samples. Therefore, the TSS powder was pressed into sheets ($d < 4\text{ mm}$) on 769YP-24B tablet compressing machine (Tianjin, China) with a $\Phi 20\text{ mm}$ mold under 30 MPa pressure.

Results and discussion

Morphology and crystal structure of TSS powder

The SEM images of uncoated TiO_2 and TSS and TEM images of TSS are displayed in Fig. 2. The uncoated TiO_2 particles are quasi-spheroid with a smooth surface and a particle size of about 200–300 nm (Fig. 2a). It can be observed from Fig. 2b, c that the surface of TiO_2 becomes rough, and there are numerous fine nanoparticles coated upon the outer surface of a matrix core in a dispersed state, forming a dense and continuous ATO coating layer, while the overall morphology of TiO_2 core remains unchanged. Figure 2c shows that there is a difference between the shell layer and core of the composite powder, and the thickness of coating shell is roughly 15 nm. As indicated by elemental mapping analysis (Fig. 2e–h), Ti, O, Sn and Sb elements do exist and are uniformly distributed in the powder. As shown in XPS full-scanned spectra (Figure S1), the peaks designated to Sn and Sb can be observed in both the precursor and

Figure 1 The schematic diagram of the fabrication process of $\text{TiO}_2@\text{Sb-SnO}_2$.



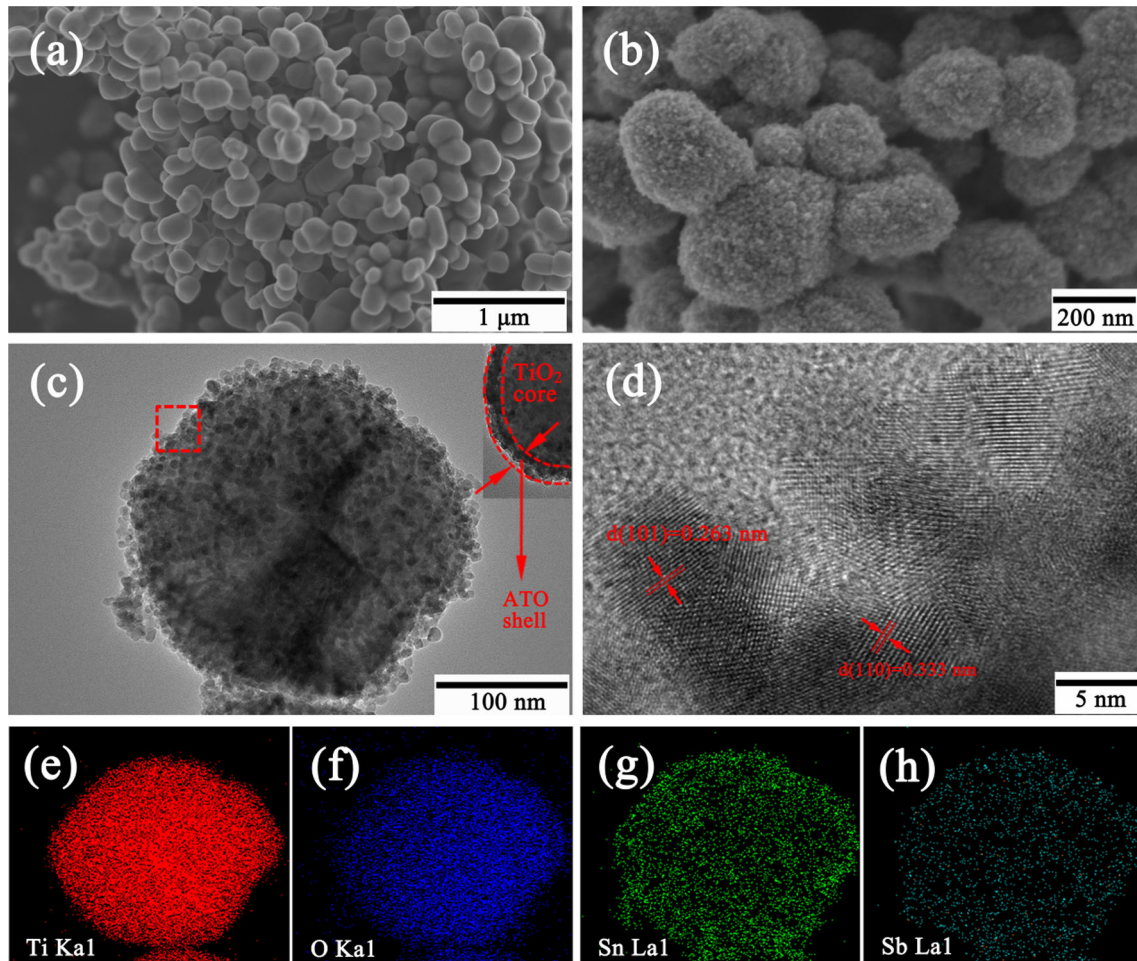


Figure 2 SEM images of **a** uncoated TiO_2 and **b** TSS; **c** TEM images of TSS; **d** HRTEM images of TSS; Elemental mapping of **e** Ti, **f** O, **g** Sn and **h** Sb.

TSS composite compared with pure TiO_2 , which confirms that there are Sn and Sb elements on the surface of TiO_2 core again. Meanwhile, the HRTEM image (Fig. 2d) of the selected area displays that the crystal plane spacing at 0.333 nm and 0.262 nm corresponds to the (110) and (101) of SnO_2 (JCPDS, No. 41-1445), respectively, which further proves that the typical core-shell structured TSS has been formed successfully.

BET method was used to measure the specific surface area of uncoated TiO_2 and TSS. The results are shown in Table 1, in which the specific surface area increased from $25.22 \text{ m}^2 \text{ g}^{-1}$ of TiO_2 to $48.11 \text{ m}^2 \text{ g}^{-1}$ of TSS with a growth rate of 190%. It indicates that the new tiny interface is formed in the material with the ATO coating on the surface of TiO_2 , leading to its surface becomes rough, which corresponds to the SEM images.

As for the conductivity of samples, the resistivity of pure TiO_2 reaches up to $45 \text{ M}\Omega \text{ cm}$ and that of ATO is $1.6 \Omega \text{ cm}$. After coating the conductive shell of ATO on TiO_2 core by homogeneous precipitation method, the as-prepared TSS composite has the improved conductivity with resistivity of about $4.0 \Omega \text{ cm}$. For another, concerning that the light colored requirement for the final product, the whiteness value (L^*) of three samples (TiO_2 , TSS and ATO) was tested by brightness tester. L^* represents the change from bright ($L^* = 100$) to dark ($L^* = 0$) of the different samples. The actual colors of three samples are shown in Fig. S2. The L^* of uncoated TiO_2 is 98.34, almost pure white, while that of ATO with deep green is 49.21. The L^* of greyish TSS conductive composite is reduced to 86.79, which meets the whiteness demand of 70–95 for inorganic filler.

Table 1 Whiteness value, specific surface area and resistivity of different samples

Sample	Whiteness value (L^*)	Specific surface area ($m^2 g^{-1}$)	Resistivity (Ωcm)
TiO ₂	98.34	25.22	4.5×10^7
TSS	86.79	48.11	4.0
ATO	49.21	–	1.6

Figure 3 exhibits the XRD patterns of uncalcined precursor and TSS at different calcination temperature. As shown in Fig. 3a, b, the characteristic peaks of all samples obviously appear at 2θ in 27.4° , 36.1° , 41.2° , 54.3° , 56.3° and 68.9° , which correspond to (110), (101), (111), (211), (220) and (301) crystal planes of rutile TiO₂ (JCPDS, No. 87-0920), respectively. After calcining, diffraction peaks at (110), (101), (211) and (200) are assigned well to the tetragonal crystalline phase of SnO₂ (JCPDS, No. 41-1445), but

diffraction peaks of related antimony compounds phases, such as Sb₂O₃ or Sb₂O₅, are not observed in any of the samples, which indicates that Sb ions is completely doped into the SnO₂ with generating interstitial or substitutional solid solution [11]. However, the uncalcined precursor only has characteristic peaks of TiO₂ matrix and unobvious diffraction peak of SnO₂. The results revealed that TiO₂ is coated with amorphous precipitates during the coating process. The peaks of SnO₂ became sharper and more intense with the increase of calcination temperature at the same calcination time (Fig. 3b), indicating that there is the higher degree of crystallinity with the calcination.

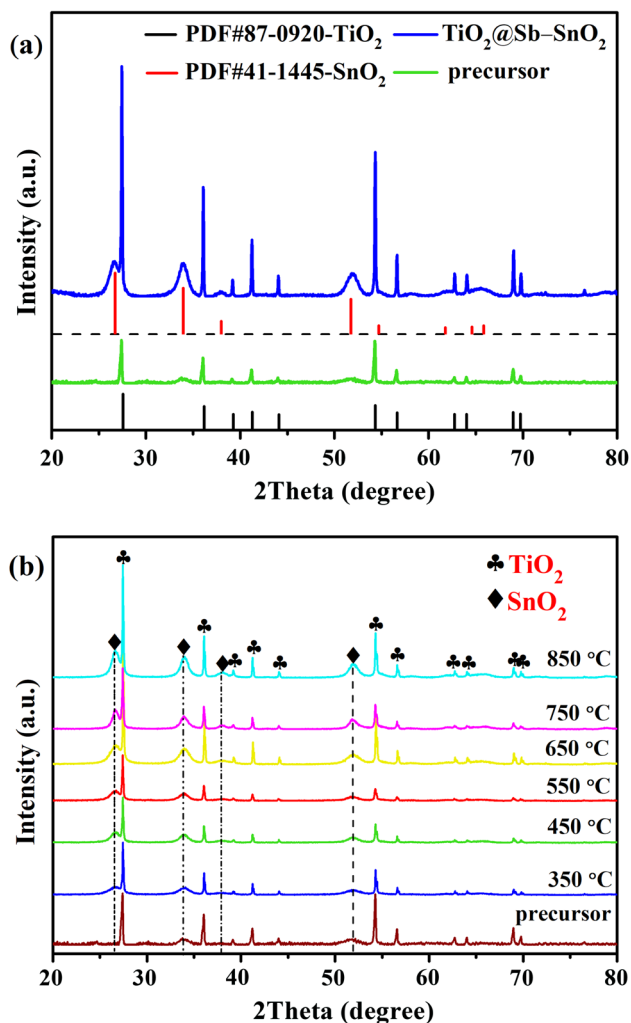


Figure 3 XRD patterns of **a** uncalcined precursor as well as TSS and **b** TSS at different calcination temperature.

Calcination action analysis

The first process of the preparation of TSS conductive powder was to form the precursor, whose nucleus was coated with a layer of precipitate at low temperature, in which part of Sb(III) in the shell layers was transformed into Sb(V), but the doped crystalline metal oxide was not formed [32]. Figure 4 shows TG analysis (TGA) curves of drying precursor powders under atmosphere of N₂ and air, respectively. The weightlessness trends of the two curves are similar. The TGA curve under air atmosphere, for example,

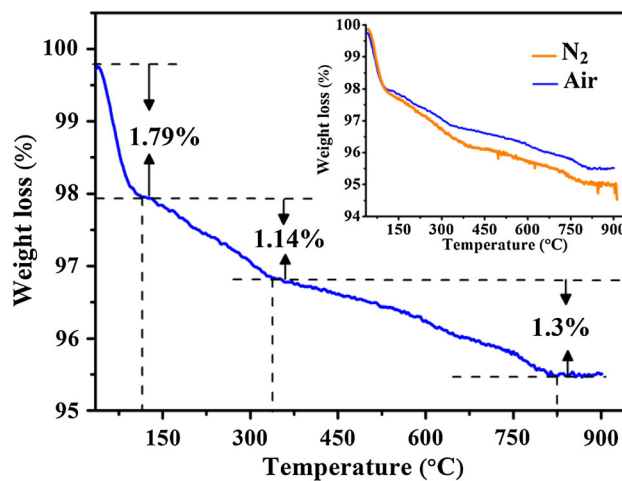


Figure 4 TG analysis of the precursor.

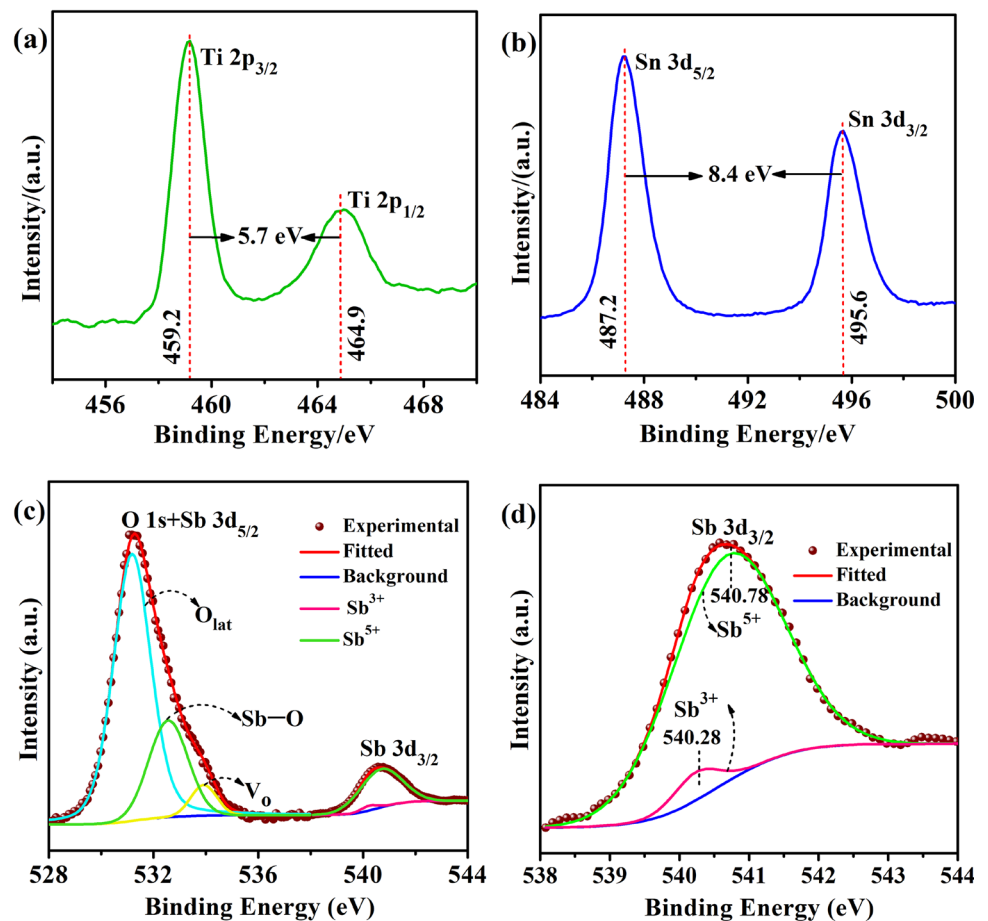
shows three-step weight loss. The precursor powder loses 1.79% of its mass below 130 °C, including adsorbed water. The second weight loss rate is 2.93% up to 350 °C, and there are water loss reactions, mainly referring to $\text{Sn}(\text{OH})_4/\text{SnO}_2 \cdot x\text{H}_2\text{O} \rightarrow \text{SnO}_2$, $\text{Sb}(\text{OH})_3 \rightarrow \text{SbO}(\text{OH}) \rightarrow \text{Sb}_2\text{O}_3$, and pyrolysis reactions of the residuals in the precursor [33]. The precursors continue to lose 1.3% of its mass when heated from 350 to 800 °C. Mostly Sb^{3+} transfer to Sb^{5+} between 400 and 600 °C, whereas Sb^{5+} is gradually reduced to Sb^{3+} to some extent when the temperature exceeds 600 °C, and Sb^{3+} is still doped in the SnO_2 lattice [34]. The particles of coating shell layer have transformed into stable metallic oxide until 800 °C, meanwhile there is no phase transformation with the core remaining rutile TiO_2 phase. That is the reason why the mass of samples remains unchanged above 800 °C.

Figure 5a shows that there are two fitted characteristic peaks for the Ti 2p spectrum and the splitting energy between Ti 2p_{3/2} and Ti 2p_{1/2} is 5.7 eV, which indicates that Ti exists in the valence state of Ti(IV) in

the TSS [35, 36], no valence state change of Ti under the action of calcination. The Sn 3d_{5/2} and Sn 3d_{3/2} spin-orbital spectrum (Fig. 5b) of TSS composite also presents characteristic double peaks. The separation between them is 8.4 eV, which agrees well with the previously reported results [11], suggesting a normal state of Sn(IV) in the TSS composite, likewise, no chemical state variation of Sn element.

In Fig. 5c, there is the overlap between O 1s and Sb 3d_{5/2} lines, including the lattice oxygen species (O_{lat}) of metallic oxides (e.g., TiO_2 or SnO_2) [37] and the peak assigned to Sb–O. Furthermore, the fitted oxygen vacancy peak can also be seen in the O 1s peak of TSS (Fig. 5c). It is worth noting that the indicator value of the g peak at 2.000 corresponds to oxygen vacancies in the SnO_2 lattice of ATO nanoshells [38], whereas the uncalcined precursor has no ESR signal (Fig. 6). Therefore, the analysis of XPS and ESR all indicate that defect reactions occur, accompanied by generating oxygen vacancies during the calcining process of the precursor. Because of the close size of ionic radius between Sb^{5+} (0.62 Å) and Sb^{4+} (0.71 Å),

Figure 5 High-resolution XPS spectra of **a** Ti 2p, **b** Sn 3d, **c** O 1s and Sb 3d and **d** Sb 3d_{3/2} for TSS composite.



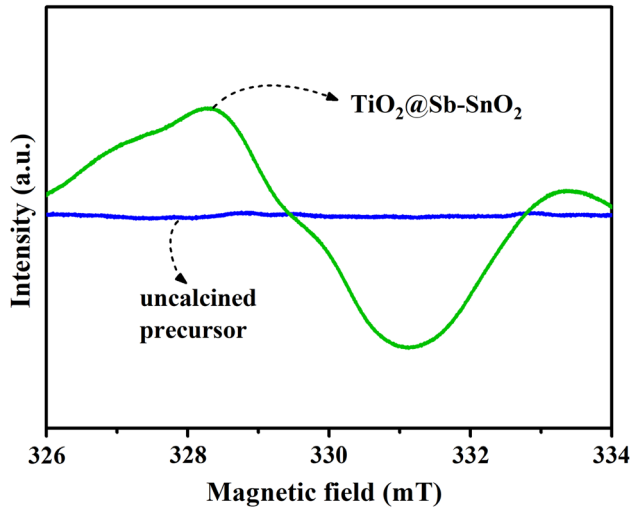
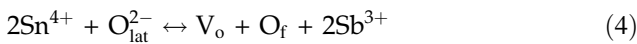
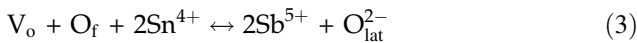
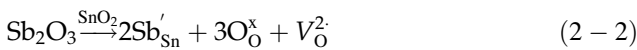
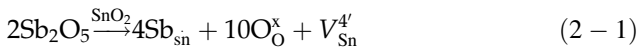


Figure 6 ESR spectra of TSS before and after calcining.

Sb⁵⁺ can form Sb–O–Sn bonds in the lattice of SnO₂, resulting in certain SnO₂ crystal deformations [39]. The main reaction equations are as follows:



Moreover, it can be seen from the fitted peak of Sb 3d_{3/2} (Fig. 5d) that there are two valence states of Sb in the shell layer of TSS, and the peak area of Sb⁵⁺ is much larger than that of Sb³⁺, which verifies that there is the competitive reaction between Sb³⁺ and Sb⁵⁺, mainly Sb⁵⁺ in the ATO shell. That is the reason why the ATO-coated composite powder has conductive property. The conductive process depends on the lattice defect of the coated particles [15] and the doped Sb⁵⁺ impurity that forms the donor levels [40] in the forbidden band of SnO₂ with free electron carriers being provided to the conduction band. After calcining, the color of samples varies from yellow to light gray, which is ascribed to the plasma absorption of electrons in the free conduction band [41].

Electrical conductivity of TSS and optimal process parameters

Electrical conductivity of TSS can be distinctly affected by preparation parameters. We mainly investigated the impacts of dropping conditions, introducing sulfate, pH value, calcination temperature and holding time on the resistivity of TSS to select optimal process parameters in this work. The influence of each parameter was investigated by varying it in the case of other parameters unchanged.

Effect of dropping conditions on resistivity

The integrity of CS structure and size of particles in the shell layer are affected by dropping temperature (*T_d*) and dropping rate (*v_d*). There is no hydrolysis of urea when the temperature is below 60 °C. The low concentration of OH⁻ in the system under this temperature results in less nucleation in the early stage and less effective coating on the surface of TiO₂, so the resistivity (*ρ*) of composite powder is higher while adding Solution B into Suspension A at 55 °C (Fig. 7, *T_d*-*ρ*). Above 60 °C, the *ρ* of TSS is gradually raised, since metal cations are not firmly adsorbed on the surface of TiO₂ under higher temperature, which contributes to part of Sn⁴⁺ and Sb³⁺ self-nucleation. In addition, the hydrolysis rate of urea increases as raising the temperature (> 60 °C), so the growth rate of crystal nuclei depends upon the hydrolysis rate of urea and the temperature. In the process, the increase of the temperature slows down the nucleation rate together with the expedited growth rate of crystal

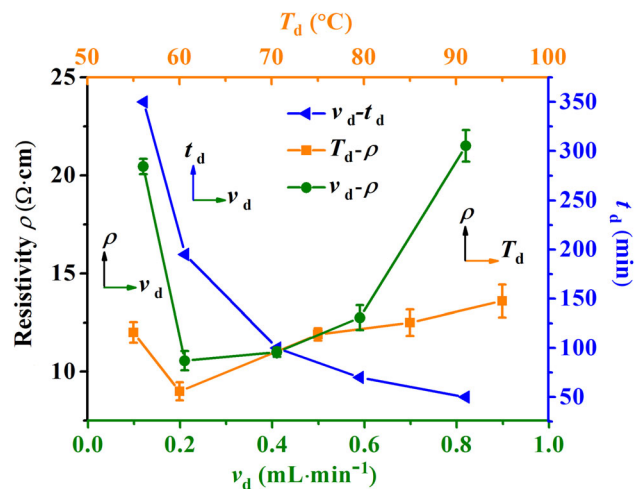


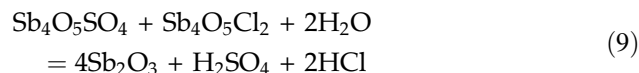
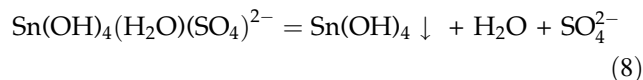
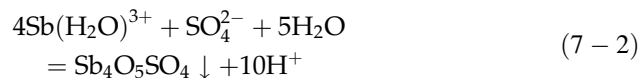
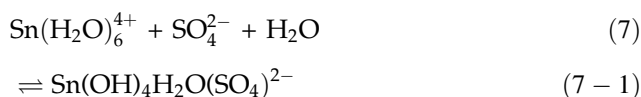
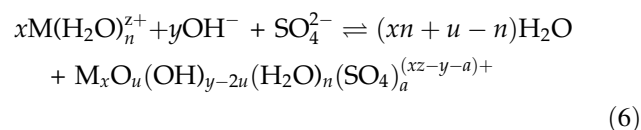
Figure 7 Effect of dropping conditions on the resistivity of TSS.

nuclei. Uniform particles in the coating layer are formed, which improves the conductivity of composite powder, when the nucleation rate is faster than the growth rate of nuclei at 60 °C.

The nucleation rate is much slower than the growth rate due to the low relative saturation of the Sn^{4+} and Sb^{3+} in the system under the condition of the slow dropping rate. As a result, the particle size of the coated layer is larger. The relative saturation of the metal cations increases rapidly at the raising rate of adding covered agent. The nucleation and growth of coated particles are not completely independent, resulting in uneven grain size and agglomeration of particles. Effective control of drop velocity can reduce or eliminate the occurrence of conglomeration of coated particles in the shell layer. The spherical particles with uniform size are evenly distributed and well dispersed, forming TSS with low ρ at the dropping rate range of 0.2–0.4 mL min^{-1} (Fig. 7, $v_d-\rho$), which is largely put down to the great consistency of the growth of nuclei in all directions. Moreover, considering that the required time of feeding (t_d) at the drip speed of 0.2 mL min^{-1} is much longer than that of 0.4 mL min^{-1} (Fig. 7, v_d-t_d), so the optimum dropping rate is 0.4 mL min^{-1} under adding temperature of 60 °C.

Effect of introduction of sulfate ions on size and resistivity

In the preparation process of TSS, the moderate amounts of sulfate radicals (SO_4^{2-}) introduced can become the induction center of nucleation within a wide pH range during the whole process of homogeneous precipitation and activate the reaction precursor. Multiple sulfate radicals are connected with each other to form two or multiple nuclei [42]. The free-energy barrier of nucleation of Sn^{4+} and Sb^{3+} can be reduced by forming new nucleation complexes with SO_4^{2-} . The process is illustrated as follows:



Hydroxyl and chlorine ions in the system cannot be coordinated with metal cations to form stable nucleation precursor complexes without adding sulfate inducer. There was only one nucleation outburst in the system with rapidly producing a large number of small nuclei. Therefore, the precursors formed are colloidal, which makes filtration and washing difficult. There remains a large amount of chlorine ions in the filter cake, so it gets hard after drying. The introduction of SO_4^{2-} significantly improves the above-mentioned conditions.

Considering that parts of sulfate, such as $\text{Al}_2(\text{SO}_4)_3$ and ZnSO_4 , will be hydrolyzed into impurity precipitates, Na_2SO_4 , K_2SO_4 and $(\text{NH}_4)_2\text{SO}_4$ are selected as the alternatives of sulfate in this experiment. The best mole ratio of SO_4^{2-} to Cl^- is always 25 among these three sulfates (Fig. 8). However, the potassium ion (K^+) or sodium ion (Na^+) introduced will destroy the photoelectric performance of the product [17, 43]. Moreover, the radius of K^+ is bigger than Na^+ , so the destructive effects on the conductive properties of the TSS may be stronger. Therefore, the electrical conductivity of the composite powder prepared by

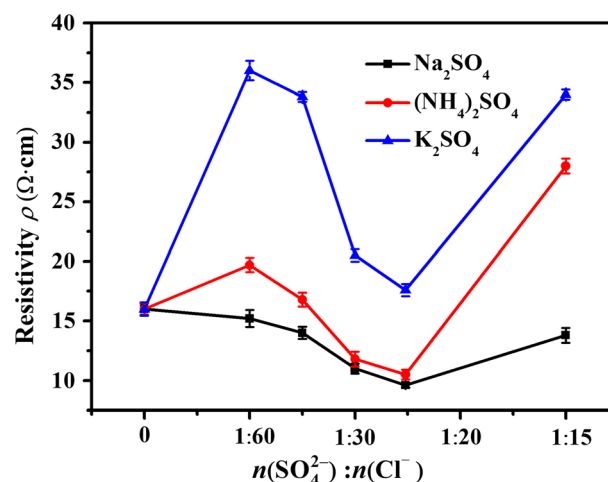


Figure 8 Resistivity of TSS at different kinds and amounts of sulfate.

adding K_2SO_4 is worse than that of not adding sulfate. As for $(NH_4)_2SO_4$, increasing the quantity of ammonium ion (NH_4^+) can inhibit the hydrolysis of urea, and the effect of NH_4^+ is greater than that of SO_4^{2-} when adding a small amount or a large amount of $(NH_4)_2SO_4$, making the ρ of the TSS powder as-prepared higher. Significant synergy effects between NH_4^+ and SO_4^{2-} may increase the conductivity of TSS under the proper amount of $(NH_4)_2SO_4$. In addition, according to the Darjaguin, Landon, Verwey and Overbeek (DLVO) theory, the soluble sulfate can be used as electrostatic stabilizers, hindering the preferential aggregation of coated particles on the surface of particles [44, 45]. The electric double layer is formed with the charge on the surface of the particles increasing. There is electrostatic repulsion between particles, so as to realize a stable dispersion of particles in the reaction mixture.

What is more, suitable $(NH_4)_2SO_4$ can also keep the growth of the nuclei at the same rate during in different directions, so it is easy to obtain more regular spherical-coated particles [45]. Figure 9 illustrates the particle size distribution of composite particles is narrow when the mole ratio of SO_4^{2-} to Cl^- is 25. When not adding or introducing small amounts of SO_4^{2-} , the size distribution range of composite powder is larger, which can be ascribed to uncertainty of central nuclear points formed by SO_4^{2-} multipoint connection. Although the kinetic salt effect becomes very weak in neutral and acidic solution, too much SO_4^{2-} may still cause a partial shedding of precipitate

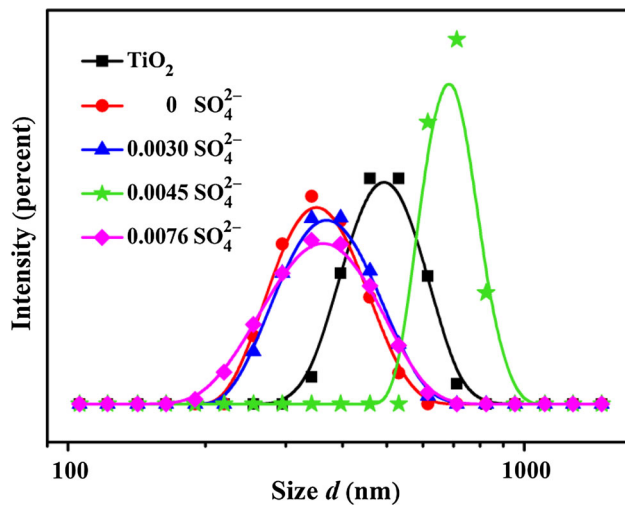


Figure 9 Size of TSS at different addition amounts of sulfate radical.

and coagulation of colloids to a certain extent, so that it leads to wide size distribution and high resistivity of TSS. Therefore, the best molar ratio of SO_4^{2-} to Cl^- is 25 with ammonium sulfate being used as the source of sulfate radicals.

Effect of pH value on Zeta potential and resistivity

As shown in Fig. 10a, when Solution B is added dropwise to the mixture under the temperature of 60 °C [46], the pH value of the system quickly falls to 1–2. After adding Solution B completely, the temperature rises to 95 °C and is retained for 7 h. In this condition, pH maintains at 1.5–2.5. When the reaction time prolongs to 7.5–8 h, the pH alters to 5–6 and reaches to 7–8 invariably as the reaction time is further extended.

In order to maintain the same dispersion condition as the reaction system to evaluate Zeta potential of TiO_2 at different pH value, 0.075 wt% CTAB, which is used as long-chain surfactant to generate weak agglomerated or mono-dispersed particles due to its steric hindrance effect [47], was added into 2.5 wt% TiO_2 slurry with 4 M hydrochloric acid and 4 M ammonia solution being added to modulate the pH of the dispersion medium. As Fig. 10b shows, the absolute value of ζ at the pH range of 1.5–2.5 is

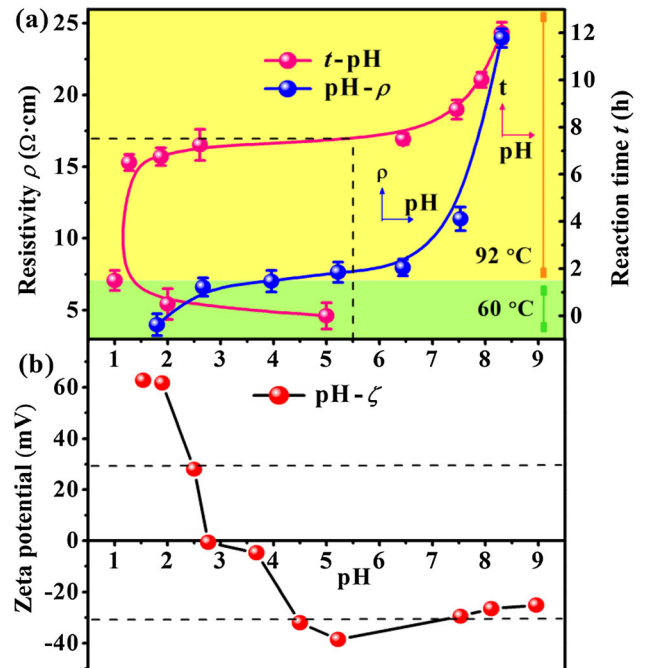


Figure 10 a Resistivity and reaction time of TSS and b Zeta potential of TiO_2 at different pH value.

greater than 30 mV [47], indicating that TiO₂ has good dispersion in the aqueous solution under this condition, which is conducive to form the uniform coating on TiO₂ particles. Furthermore, the starting pH for forming Sn(OH)₄ is about 0.22 and the complete precipitation pH of Sn(OH)₄ is approximately 2.88. The range of precipitation pH of Sb(OH)₃ is from 1.60 to 4.30. Therefore, when the pH value of the system is 1.5–2.5, Sn⁴⁺ and Sb³⁺ ions can be basically hydrolyzed synchronously as the adsorption of hydrolysis products on TiO₂ surface. Meanwhile, the ρ value of the prepared composite powder is the lowest (Fig. 10a). The ρ of composite powder increases slowly with the increase of the terminal pH value at the range of 2.5–6.5 because the absolute value of ζ is less than 30 mV, and TiO₂ powder is easily agglomerated under the condition, leading to the incomplete coating of the hydrolysate. Although TiO₂ powder is in a good dispersion state when pH = 4.5–6.5, Sn⁴⁺ and Sb³⁺ ions are almost completely precipitated, the ρ of composite powder changes little. The partial separation and dissolution of the coating layer occur under the alkaline environment [40], which is the reason why the ρ of TSS increases sharply when the terminal pH varies from approximately 6.5–8.0. Above all, the optimum to prepare precursor composite is that the mixture is stirred for 5.5 h at 95 °C maintaining the pH at 1.5–2.5 after adding the whole capping agent.

Effect of calcination conditions on resistivity

According to the results of TGA, the calcination temperature was selected from 350 to 850 °C. As shown in Fig. 2b, the crystallinity of the precursor gets higher with the rise of calcination temperature. As a consequence, the ρ of the composite powder decreases slowly with it, and it reaches to the lower value at the range of 550–600 °C (Fig. 11). Above 600 °C, the ρ of composite powder shows a slow rising trend mainly because Sb⁵⁺ begins to change into Sb³⁺, which corresponds to TGA, and the coating may burst at high temperature. Moreover, there is also Sb segregation occurs on the crystal surface, hindering carrier migration,

At the calcination temperature of 550 °C, the ρ of TSS decreases significantly with the extension of calcination time, whereas the ρ increases slowly when the calcination time exceeds 2.5 h. In addition, the longer calcination time make the coated particles

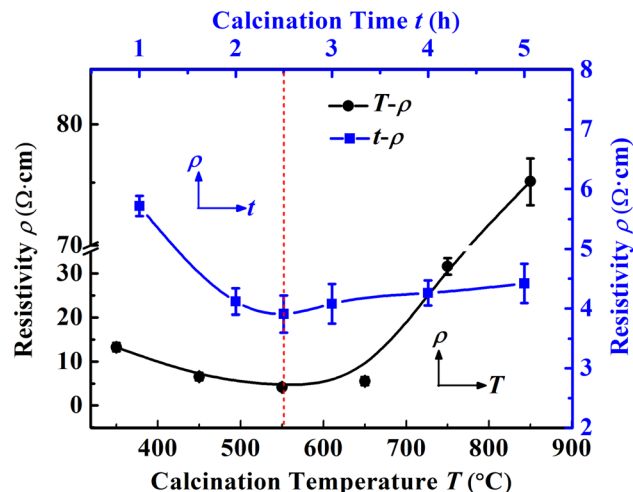


Figure 11 Resistivity of TSS at different calcination temperature and time.

get coarsened, causing the waste of energy. What is worse, there is little significance for the improvement of its electrical conductivity. Lower calcination temperature and shorter calcination time lead to the poor conductivity of TSS powder because only the adsorbed water is taken off the precursor. In other words, there is no transformation or the incomplete transformation of crystal structure, as well as a low concentration of Sb⁵⁺ and few doping defects in coating layer. In conclusion, the obtained TSS has excellent conductivity, with the ρ of about 4.0 Ω cm, when the as-prepared precursor is calcined at the optimum calcination temperature from 550 to 600 °C for 2.5 h.

Conductive mechanism analysis

According to the formula of composite powder resistance [40]:

$$R = \sum R_g + \sum R_c + \sum R_b \quad (10)$$

where $\sum R_b$ and $\sum R_c$ are the self-resistance and contact resistance of conductive particles, respectively, and $\sum R_g$ is the interface resistance in contact with the substrate. The self-resistance of the coated particles is negligible. The different contact states of particles in the shell layer correspond to three equivalent circuit diagrams, respectively, as displayed in Fig. 12.

- (I) The conductive particles on the surface of TiO₂ are discontinuous. Composite particles can be considered as an electrical insulator

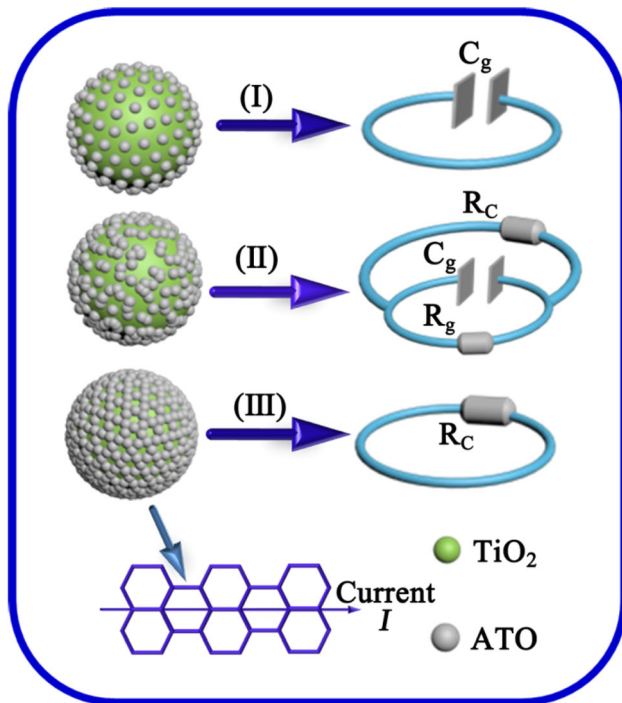


Figure 12 Three contact states and equivalent circuits of coated particles.

equivalent to the capacitor effect, which have weak capacitive conductivity.

- (II) The coated conductive particles are not completely continuous, in which the non-contacting conductive particles form a current path due to the tunnel effect, corresponding to the resistance R_g and the capacitor C_g connected in parallel and then in series with the resistor R_c .
- (III) The particles in the coating layer contact with each other continuously to form a current path, which is equivalent to the current flowing through a resistance R_c .

There may be three kinds of conductive mechanisms in the TSS composite conductive materials, including the tunnel effect [48], field emission [49] and conductive channel [50] mechanism. Under the condition of low content of ATO (I), the effect of field emission mechanism on the conductivity of the composite becomes significant. The distance between conductive-coated particles of the as-prepared composite is small, mainly forming chain-like conductive channels (III). The conductive channel mechanism plays a leading role. The conductive particles are distributed on the surface of the substrate, a

honeycomb or network of conductive networks can be formed (Fig. 12), so the whole composite system is conductive and the purpose of conducting current and eliminating accumulated static charge can be achieved.

Conclusions

In this work, we successfully prepared the core-shell structured TSS via homogeneous precipitation with heat treatment method using urea as appropriate homogeneous precipitant. In the process, coating solution containing tin and antimony ions was added dropwise at a speed of 0.4 mL min^{-1} into the TiO_2 matrix Suspension at 60°C . Meantime, $(\text{NH}_4)_2\text{SO}_4$ was used as nucleating agent and electrostatic stabilizers, as well as CTAB as dispersant. Following experiment began at 95°C for 5.5 h, controlling the pH value of terminal point at 1.5–2.5. The obtained precursors were finally calcined at 550°C for 2.5 h in the air to synthesis the composite powder with good conductivity, whose resistivity is below $4.0 \Omega \text{ cm}$ and the specific surface area has been increased from $25.22 \text{ m}^2 \text{ g}^{-1}$ to $48.11 \text{ m}^2 \text{ g}^{-1}$. Furthermore, the material in a shell of the precursor was calcined to form the shell of antimony-doped tin oxide, in which defect reactions occurred, and Sb was doped into the SnO_2 lattice with generating free electron carriers and oxygen vacancies, while forming interstitial or substitutional solid solution. ATO particles contact with each other on the surface of TiO_2 to form a conductive path. This present method provides a novel idea for low cost preparation of TiO_2 or mineral-matrix light color composite conductive powder and other core-shell functional composite materials.

Acknowledgements

This work was financially supported by National Natural Science Foundation of China (No. 21878024) and Innovation Team Project of Liaoning Province (Nos. LT2015001 and 2018479-14).

Electronic supplementary material: The online version of this article (<https://doi.org/10.1007/s10853-019-04229-6>) contains supplementary material, which is available to authorized users.

References

- [1] Purbia R, Paria S (2015) Yolk/shell nanoparticles: classifications, synthesis, properties, and applications. *Nanoscale* 7:19789–19873
- [2] Bayal N, Jeevanandam P (2012) Synthesis of CuO@NiO core-shell nanoparticles by homogeneous precipitation method. *J Alloy Compd* 537:232–241
- [3] Kusiora A, Zycha L, Zakrzewskab K, Radecka M (2019) Photocatalytic activity of TiO₂/SnO₂ nanostructures with controlled dimensionality/complexity. *Appl Surf Sci* 471:973–985
- [4] Jia B, Cao P, Zhang H, Wang G (2019) Mesoporous amorphous TiO₂ shell-coated ZIF-8 as an efficient and recyclable catalyst for transesterification to synthesize diphenyl carbonate. *J Mater Sci* 54:9466–9477. <https://doi.org/10.1007/s10853-019-03595-5>
- [5] Yang S, Huang Y, Han G, Liu J, Cao Y (2017) Synthesis and electrochemical performance of double shell SnO₂@amorphous TiO₂ spheres for lithium ion battery application. *Powder Technol* 322:84–91
- [6] Zhang Q, Zhang W, Peng K (2019) In-situ synthesis and magnetic properties of core-shell structured Fe/Fe₃O₄ composites. *J Magn Magn Mater* 484:418–423
- [7] Zheng C, Wang Y, Phua SZF, Lim WQ, Zhao Y (2017) ZnO-DOX@ZIF-8 core-shell nanoparticles for pH-responsive drug delivery. *ACS Biomater Sci Eng* 3:2223–2229
- [8] Zhang S, Chen S, Yang F et al (2019) High-performance electrochromic device based on novel polyaniline nanofibers wrapped antimony-doped tin oxide/TiO₂ nanorods. *Org Electron* 65:341–348
- [9] Li N, Li Y, Li W, Ji S, Jin P (2016) One-Step hydrothermal synthesis of TiO₂@MoO₃ core-shell nanomaterial: Microstructure, growth mechanism, and improved photochromic property. *J Phys Chem C* 120:3341–3349
- [10] Du Y, Yan J, Meng Q, Wang J, Dai H (2012) Fabrication and excellent conductive performance of antimony-doped tin oxide-coated diatomite with porous structure. *Mater Chem Phys* 133:907–912
- [11] Hu Y, Zhong H, Wang Y, Lu L, Yang H (2018) TiO₂/antimony-doped tin oxide: Highly water-dispersed nanocomposites with excellent IR insulation and super-hydrophilic property. *Sol Energy Mater Solar Cells* 174:499–508
- [12] Zhao N, He C, Liu J et al (2014) Dependence of catalytic properties of Al/Fe₂O₃ thermite on morphology of Fe₂O₃ particles in combustion reactions. *J Solid State Chem* 219:67–73
- [13] Li YQ, Mei SG, Byon YJ, Wang JL, Zhang GL (2013) Highly solar radiation reflective Cr₂O₃-3TiO₂ orange nanopigment prepared by a polymer-pyrolysis method. *ACS Sustain Chem Eng* 2:318–321
- [14] Hu P, Yang H, Ouyang J (2012) Synthesis and characterization of Sb-SnO₂/kaolinites nanoparticles. *Appl Clay Sci* 55:151–157
- [15] Wang LS, Lu HF, Hong RY, Feng WG (2012) Synthesis and electrical resistivity analysis of ATO-coated talc. *Powder Technol* 224:124–128
- [16] Hu Y, Zhang H, Yang H (2008) Synthesis and electrical property of antimony-doped tin oxide powders with barite matrix. *J Alloy Compd* 453:292–297
- [17] Li X, Qian JH, Xu JS, Sun YD, Liu L (2019) Synthesis and electrical properties of antimony-doped tin oxide-coated TiO₂ by polymeric precursor method. *Mat Sci Semicon Proc* 98:70–76
- [18] Yu H, Chen F, Ye L, Zhou H, Zhao T (2019) Enhanced photocatalytic degradation of norfloxacin under visible light by immobilized and modified In₂O₃/TiO₂ photocatalyst facilely synthesized by a novel polymeric precursor method. *J Mater Sci* 54:10191–10203. <https://doi.org/10.1007/s10853-019-03636-z>
- [19] Sladkevich S, Kyi N, Gun J, Prikhodchenko P, Ischuk S, Lev O (2011) Antimony doped tin oxide coating of muscovite clays by the Pechini route. *Thin Solid Films* 520:152–158
- [20] Liu H, Zhang J, Gou J, Sun Y (2017) Preparation of Fe₂O₃/Al composite powders by homogeneous precipitation method. *Adv Powder Technol* 28:3241–3246
- [21] Montañez MK, Molina R, Moreno S (2014) Nickel catalysts obtained from hydrotalcites by coprecipitation and urea hydrolysis for hydrogen production. *Int J Hydrogen Energy* 39:8225–8237
- [22] Villegas M, Sierra T, Caballero AC, Fernandez JF (2007) Ti-based nanocoatings on Al₂O₃ powders. *Ceram Int* 33:875–878
- [23] Yang Z, Qi Y, Zhang J (2019) A novel perspective for reflective cooling composites: influence of the difference between the effective refractive index of polymeric matrix and inorganic functional particles. *Constr Build Mater* 223:928–938
- [24] Schwindt N, Pidoll U, Markus D, Klausmeyer U, Papalexandris MV, Grosshans H (2017) Measurement of electrostatic charging during pneumatic conveying of powders. *J Loss Prev Proc* 49:461–471
- [25] Wang C, Wang D, Yang R, Wang H (2019) Preparation and electrical properties of wollastonite coated with antimony-doped tin oxide nanoparticles. *Powder Technol* 342:397–403
- [26] Li X, Qian JH, Xu JS, Xing JJ, Tao E (2018) Synthesis, characterization and electrical properties of TiO₂ modified with SiO₂ and antimony-doped tin oxide. *J Mater Sci Mater El* 29:12100–12108

- [27] Heller A, Jarvis K, Coffman SS (2018) Association of type 2 diabetes with submicron titanium dioxide crystals in the pancreas. *Chem Res Toxicol* 31:506–509
- [28] Wang Y, Jamal R, Wang M, Yang L, Liu F, Abdiryim T (2017) A donor-acceptor-donor-type conjugated polymer-modified TiO₂ with enhanced photocatalytic activity under simulated sunlight and natural sunlight. *J Mater Sci* 52:4820–4832. <https://doi.org/10.1007/s10853-016-0717-7>
- [29] Redmond PL, Hallock AJ, Brus LE (2005) Electrochemical ostwald ripening of colloidal Ag particles on conductive substrates. *Nano Lett* 5:131–135
- [30] Chung DDL (2001) Electromagnetic interference shielding effectiveness of carbon materials. *Carbon* 39:279–285
- [31] Flahaut E, Peigney A, Laurent C, Marlière C, Chastel F, Rousset A (2000) Carbon nanotube-metal-oxide nanocomposites: microstructure, electrical conductivity and mechanical properties. *Acta Mater* 48:3803–3812
- [32] Rockenberger J, Uz F, Tischer M, Tröger L (2000) Near edge X-ray absorption fine structure measurements and extended X-ray absorption fine structure measurements of the valence state and coordination of antimony in doped nanocrystalline SnO₂. *J Chem Phys* 112:4292–4304
- [33] Siciliano P (2000) Preparation, characterisation and applications of thin films for gas sensors prepared by cheap chemical method. *Sens Actuat B Chem* 70:153–164
- [34] Sun K, Liu J, Browning ND (2002) Correlated atomic resolution microscopy and spectroscopy studies of Sn(Sb)O₂ nanophase catalysts. *J Catal* 205:266–277
- [35] Tian BZ, Li CZ, Zhang JL (2012) One-step preparation, characterization and visible-light photocatalytic activity of Cr-doped TiO₂ with anatase and rutile bicrystalline phases. *Chem Eng J* 191:402–409
- [36] Wan HC, Yao WT, Zhu WK, Tang Y, Ge HL, Shi XZ, Duan T (2018) Fe-N co-doped SiO₂@TiO₂ yolk-shell hollow nanospheres with enhanced visible light photocatalytic degradation. *Appl Surf Sci* 444:355–363
- [37] Li XY, Wu Y, Zhu W, Xue FQ, Qian Y, Wang CW (2016) Enhanced electrochemical oxidation of synthetic dyeing wastewater using SnO₂-Sb-doped TiO₂-coated granular activated carbon electrodes with high hydroxyl radical yields. *Electrochim Acta* 220:276–284
- [38] Ou G, Xu Y, Wen B et al (2018) Tuning defects in oxides at room temperature by lithium reduction. *Nat Commun* 9:1302–1310
- [39] Cui YH, Feng YJ, Liu ZQ (2009) Influence of rare earths doping on the structure and electro-catalytic performance of Ti/Sb-SnO₂ electrodes. *Electrochim Acta* 54(21):4903–4909
- [40] Hu P, Yang H (2010) Controlled coating of antimony-doped tin oxide nanoparticles on kaolinite particles. *Appl Clay Sci* 48:368–374
- [41] Baena JPC, Agrios AG (2014) Transparent conducting aerogels of antimony-doped tin oxide. *ACS Appl Mater Interfaces* 6:19127–19134
- [42] Hek HD, Stol RJ, Bruyn PLD (1978) Hydrolysis-precipitation studies of aluminum(III) solutions. 3. The role of the sulfate ion. *J Colloid Interf Sci* 64:72–89
- [43] Colemana JP, Freeman JJ, Madhukar P, Wagenknecht JH (1999) Electrochromism of nanoparticulate-doped metal oxides: optical and material properties. *Displays* 20:145–154
- [44] Wen L, Sun X, Xiu Z, Chen S, Tsai C-T (2004) Synthesis of nanocrystalline yttria powder and fabrication of transparent YAG ceramics. *J Eur Ceram Soc* 24:2681–2688
- [45] Lv Y, Zhang W, Liu H, Sang Y, Qin H, Tan J, Tong L (2012) Synthesis of nano-sized and highly sinterable Nd:YAG powders by the urea homogeneous precipitation method. *Powder Technol* 217:140–147
- [46] Tan J, Shen L, Fu X, Hou W, Chen X (2004) Preparation of nanometer-sized (1-x)SnO₂·xSb₂O₃ conductive pigment powders and the hydrolysis behavior of urea. *Dyes Pigm* 61:31–38
- [47] Huo W, Zhang X, Gan K, Chen Y, Xu J, Yang J (2019) Effect of zeta potential on properties of foamed colloidal suspension. *J Eur Ceram Soc* 39:574–583
- [48] Beliatas MJ, Martin NA, Leming EJ, Silva SRP, Henley SJ (2011) Laser ablation direct writing of metal nanoparticles for hydrogen and humidity sensors. *Langmuir* 27:1241–1244
- [49] Yanagi K, Udoguchi H, Sagitani S et al (2010) Transport mechanisms in metallic and semiconducting single-wall carbon nanotube networks. *ACS Nano* 4:4027–4032
- [50] Peng Q, Kalanyan B, Hoertz PG et al (2013) Solution-processed, antimony-doped tin oxide colloid films enable high-performance TiO₂ photoanodes for water splitting. *Nano Lett* 13:1481–1488

Publisher's Note Springer Nature remains neutral with regard to jurisdictional claims in published maps and institutional affiliations.